

Contents

1	Infra-red radiative cooling/heating of mesosphere and lower thermosphere due to the small-scale temperature fluctuations associated with gravity waves	1
	Alexander A. Kutepov, Artem G. Feofilov, Alexander S. Medvedev, Uwe Berger, Martin Kaufmann, and Adalbert W. A. Pauldrach	
1.1	Introduction	2
1.2	Stochastic Model of Gravity Waves	2
1.3	Infra-red Radiative Cooling/Heating of MLT	4
1.4	Calculation Procedure and Inputs	5
1.5	Results and Discussion	6
1.6	Parametrization	6
1.7	Effects of ITFs on the O ₃ and H ₂ O Cooling	9
1.8	Application in the LIMA Model	10
1.9	Conclusion	13
	References	13

Chapter 1

Infra-red radiative cooling/heating of mesosphere and lower thermosphere due to the small-scale temperature fluctuations associated with gravity waves

Alexander A. Kutepov, Artem G. Feofilov, Alexander S. Medvedev, Uwe Berger, Martin Kaufmann, and Adalbert W. A. Pauldrach

Abstract We address the effect of an additional infrared radiative cooling/heating of the mesosphere and lower thermosphere (MLT) in the infrared bands of CO₂, O₃ and H₂O due to small-scale irregular temperature fluctuations associated with gravity waves (GWs). These disturbances are not well resolved by present general circulation models (GCMs), but they alter the radiative transfer and cooling rates significantly. A statistical model of gravity wave-induced temperature variations was applied to large-scale temperature profiles, and the corresponding direct radiative calculations were performed with accounting for the breakdown of the local thermodynamic equilibrium (non-LTE). We show that temperature fluctuations can cause an additional cooling up to 4 K day⁻¹ near the mesopause. The effect is produced mainly by the fundamental 15 μ m band of the main CO₂ isotope ¹²C¹⁶O₂ (626). A simple parametrization has been derived that computes corrections depending on the temperature fluctuations variance, which need to be added in radiative calculations to the mean temperature and the volume mixing ratios (VMRs) of CO₂ and O(³P) to account for additional cooling/heating caused the unresolved distur-

Alexander A. Kutepov, Artem G. Feofilov
Department of Physics, The Catholic University of America/NASA Goddard Space Flight Center,
8800 Greenbelt Rd, Greenbelt, MD 20771-2400, USA e-mail: alexander.a.kutepov@nasa.gov

Alexander S. Medvedev
Max Planck Institute for Solar System Research, Max-Planck-Strasse 2, 37191 Katlenburg-Lindau,
Germany e-mail: medvedev@mps.mpg.de

Uwe Berger
Leibniz-Institute of Atmospheric Physics, Schlossstr. 6, D-18225 Kühlungsborn, Germany e-mail:
berger@iap-kborn.de

Martin Kaufmann
Institute for Chemistry and Dynamics of Geosphere, Forschungszentrum Jülich GmbH 52425
Jülich, Germany e-mail: m.kaufmann@fz-juelich.de

Adalbert W. A. Pauldrach
University Observatory Munich/ Wendelstein Observatory, Scheinerstr. 1, 81679 München, Ger-
many e-mail: uh10107@usm.uni-muenchen.de

bances. Implementation of this scheme into the LIMA model resulted in a colder and broader simulated summer mesopause in agreement with recent lidar measurements at Spitsbergen.

1.1 Introduction

Light absorption and scattering in the atmosphere strongly depend on distributions of temperature and radiatively active constituents. In the middle atmosphere, instantaneous profiles are highly irregular due to disturbances associated with small-scale gravity waves (GWs). These waves with vertical wavelengths $\lambda_z \ll 2\pi H$, H being a scale height, are dynamically extremely important in the mesosphere and lower thermosphere (MLT). Because they are not well resolved by contemporary general circulation models (GCMs), their effects in the atmosphere are usually accounted for in form of so-called “GW drag” parametrization (*Fritts and Alexander, 2003*, and references therein). The influence of these subgrid-scale GW disturbances on radiative transfer and the related heating/cooling is always missing in GCMs mainly because of the two reasons: 1) GWs are not well resolved – $2\delta z$ -harmonics are not reproduced, 3 to 4- δz waves are resolved poorly because of the numerical and physical diffusion at small scales, and only harmonics with $\lambda_z \geq 5\delta z$ can be considered as resolved by GCMs; 2) Parametrization of radiative heating and cooling normally perform calculations at grids even sparser than the model resolution, followed by an interpolation onto the model grid.

In this study we estimate the effect of the subgrid temperature fluctuations T' on the infrared radiative cooling/heating of MLT. Sec. 1.2 outlines the model of GW induced temperature and volume mixing ratio fluctuations. Infra-red radiative cooling/heating of MLT and its calculation are described in Sec. 1.3. Sec. 1.4 discusses the computational approach and inputs used in this study. The additional CO₂ cooling/heating caused by the subgrid GW-induced T' as well as its parametrization are discussed in Sec. 1.5 and Sec. 1.6, respectively. In Sec. 1.7 the effects of subgrid GWs on the the O₃ and H₂O cooling and their parametrizations are presented. The accounting for the subgrid GW CO₂ cooling in LIMA model and its impact on calculated temperatures are discussed in Sec. 1.8 The Conclusion summarizes results and provides recommendations for implementation of obtained parametrizations in GCMs.

1.2 Stochastic Model of Gravity Waves

Temperature variations associated with GW are highly complex and irregular. In many observational studies their properties are usually summarized in the form of averaged spectra. Here we applied a simplified model described below which randomly generates individual temperature profiles reminiscent of instantaneous mea-

measurements during periods of strong GW activity, whose statistical properties agree with observed GW spectra. Since individual profiles cannot be reconstructed from observed spectra, the model required additional plausible assumptions.

A vertical temperature distribution created by GW can be represented as a sum of individual harmonics:

$$T'(z) = \sum_k T_k(z) = \sum_k \hat{T}_k(z_0) \exp\left(i \int_{z_0}^z m_k(z') dz' + \phi_k\right), \quad (1.1)$$

where $\hat{T}_k(z_0)$ is the amplitude of the k -th harmonic at the source level z_0 , $m_k(z) = m_k^{(R)} + im_k^{(I)}$ is its complex vertical wavenumber, ϕ_k is the phase. This yields for each k

$$dT_k/dz = im_k T_k. \quad (1.2)$$

If $T_k(z_0)$, $m_k(z_0)$, and ϕ_k are known at the source level, (1.2) can be integrated vertically for each harmonic k to obtain the profile $T'(z)$. Real parts of the vertical wavenumbers $m_k^{(R)}$ for GW harmonics are, generally, functions of z as they depend on the refractive properties of the atmosphere determined by the background wind and temperature. However, $T_k(z)$ is not an individual plane wave, but rather a sum of GW harmonics with different phase velocities travelling at different angles to the mean wind. Here we assume no vertical dependence for $m_k^{(R)}$ since there exists no rigorous requirement for the opposite in the given formulation. This also helps to make the calculations tractable. The imaginary part of the vertical wavenumber, $m_k^{(I)}$, should include the effects of the amplification due to the air density decrease, damping by the molecular viscosity, and the effect of amplitude saturation which limits the instantaneous temperature gradients by the value of the adiabatic lapse rate, i.e., $\bar{T}_z + T'_z \geq -gc_p^{-1}$, c_p being the specific heat capacity, g is the acceleration of gravity. The first two effects enter (1.2) in the form (see e.g., *Vadas and Fritts*, 2005])

$$m_k^{(I)} = -1/2H(z) + \mu m_k^{(R)3}/(\rho\omega), \quad (1.3)$$

where H is the scale height; $\mu=0.017 \text{ gm}^{-1}\text{s}^{-1}$ is the molecular viscosity, ρ is the density, and ω is the assumed frequency of the harmonic. In our calculations, ω served as a tuning parameter to ensure that all wave disturbances dissipate above the turbopause. A “convective adjustment scheme” turns on to modify the temperature $T'(z)$ when the net vertical gradient of the potential temperature becomes negative.

We use the canonical “modified DeSaubies” vertical wavenumber spectrum to prescribe the wave field at the source level $z_0 = 15 \text{ km}$: $S(m/m_*) = A_0(m/m_*)^s [(1 + (m/m_*)^{s+3})^{-1}]$, where S is the wave spectral density, and the values for the following parameters were borrowed from [*Medvedev and Klaassen*, 2000]: $s = 0$ or 1 , $m_* = 0.006 \text{ m}^{-1}$, $A_0 = 10$ to 100 . The algorithm of the temperature profile generation is as follows. First, several vertical wavenumbers $2\pi\lambda_{max}^{-1} \leq m_k^{(R)} \leq 2\pi\lambda_{min}^{-1}$ and the corresponding phases ϕ_k are randomly generated, where λ_{max} and λ_{min} are the longest and shortest vertical wavelengths, respectively. The amplitudes of the harmonics are assigned according to the DeSaubies spectrum. Then, (1.2) is integrated

upward to produce an individual profile $T'(z)$. There is ample evidence [e.g., *Fritts and Alexander*, 2003, section 4.3] that GW spectra in the atmosphere are composed of only a few harmonics rather than represent a broad mix of waves. *Sica and Russel* [1999] argued that, in observations, the spectra most often are dominated by 1 to 3 waves. We use 2 GW harmonics in our simulations.

The following parameters have been used in the calculations presented below: the vertical grid step $\Delta z = 300$ m, $A_0 = 40$, $s = 0$, $\lambda_{max} = 11$ km, $\lambda_{min} = 2.5$ km. As there is no data on the frequency of occurrence of waves with different vertical wavenumbers in observations, we assumed the same probability for harmonics with all wavelengths.

Kutepov et al. (2007) applied the model described above in this section for investigating the additional CO_2 , O_3 and H_2O coolings of MLT due to the small-scale T' alone. Additionally to this study we investigated the combined effect on the CO_2 cooling/heating of T' , $\text{O}(^3\text{P})$ and CO_2 fluctuations. The densities of $\text{O}(^3\text{P})$ and CO_2 as conservative tracers of MLT *Brasseur and Solomon* (2005) undergo GW-induced variations due to adiabatic displacements of air parcels. Following *Ward* (1999), one can express VMR variations of these gases, $c'_{v,M}$, as functions of temperature variations T'

$$c'_{v,M} = \varepsilon_M T', \quad \varepsilon_M = \frac{dc_{v,M}}{dz} / \left(\frac{dT}{dz} + \frac{RT}{c_p H} \right), \quad (1.4)$$

where $M = \text{CO}_2$, $\text{O}(^3\text{P})$, $c_{v,M}$ and T are the mean VMR and temperature profiles, respectively, R is the gas constant, and H is the density scale height.

1.3 Infra-red Radiative Cooling/Heating of MLT

The radiative cooling of the MLT, both at day and night, is affected mainly by the vibration-rotational bands of CO_2 around $15 \mu\text{m}$. The $9.6 \mu\text{m}$ O_3 band is next in importance contributing up to 25% of the total cooling at and around the stratopause. The water vapor cooling (dominated by the H_2O rotational band) plays a tertiary role contributing about 5–7% of the total IR cooling of the MLT. At daytime, the infra-red heating of MLT is caused mostly by the CO_2 absorption of the Solar radiation in the near infrared spectral region of $1\text{--}4.3 \mu\text{m}$.

The radiative cooling/heating of the atmosphere h is described by the radiative flux divergence taken with the minus sign. Integrating the radiative transfer equation over the total solid angle Ω and frequency ν , one obtains

$$h = - \int d\Omega \int d\nu \frac{dI_{\Omega\nu}}{ds} = \chi(J - S), \quad (1.5)$$

where $I_{\Omega\nu}$ is the radiative intensity, $J = (1/4\pi\chi) \int d\Omega \int d\nu \chi(\nu) I_{\Omega\nu}$ is the mean radiative intensity, $S = \eta(\nu)/\chi(\nu)$ is the source function defined as a ratio of the atmospheric emissivity $\eta(\nu)$ and opacity $\chi(\nu)$, and $\chi = \int \chi(\nu) d\nu$ is the mean atmospheric opacity in the spectral region under consideration. χS in (1.5) describes

the radiative loss of energy by a unit volume, and χJ describes the absorption by the same unit volume of the radiation coming from other atmospheric layers, the upwelling radiation from the surface, and the solar radiation.

In the lower atmosphere, inelastic molecular collisions determine the population of molecular levels. As a result local thermodynamic equilibrium (LTE) exists, where the populations n_ν of molecular vibrational levels ν obey the Boltzmann law with the local kinetic temperature T , and S in (1.5) is equal to the Planck function $B_\nu(T)$. In the middle and upper atmosphere, the frequency of collisions is low, and other processes which populate and depopulate molecular levels (such as an absorption and emission of the radiation in molecular bands, redistribution of excitation between colliding molecules, chemical excitation, etc.) must be taken into account. Under these non-LTE conditions n_ν deviate from the Boltzmann distribution for the local T , and S is no longer equal to $B_\nu(T)$. Non-LTE n_ν are found from a set of rate equations expressing a balance of all processes, which populate and depopulate vibrational levels ν , and the radiative transfer equation in the ro-vibrational bands.

1.4 Calculation Procedure and Inputs

We used the ALI-ARMS (Accelerated Lambda Iteration for Atmospheric Radiation and Molecular Spectra) code *Kutepov et al. (1998)*, *Gusev and Kutepov (2003)* for solving the non-LTE problem and calculating the radiative cooling/heating in the CO₂ bands. 60 vibrational levels and 150 vibrational-rotational bands of four CO₂ isotopes were taken into account. They included a large number of weak combination bands that absorb the near-infrared solar radiation during day time. The set of collisionally induced vibrational-translational (V-T) and vibrational-vibrational (V-V) energy exchange processes and rate coefficients correspond to those described by *Shved et al. (1998)*.

We examined five atmospheric models corresponding to the summer solstice in the Northern hemisphere: at -70.0° for the subarctic winter (SAW), -40.0° for the midlatitude winter (MLW), 0.0° for the tropics (TROP), 40.0° for the midlatitude summer (MLS), and 70.0° for the subarctic summer (SAS). The local noons were set for each model with the Solar zenith angles equal 93.5° , 63.5° , 23.5° , 16.5° , and 46.5° , respectively. Temperature T , pressure p , $[N_2]$, $[O_2]$ and $[O(^3P)]$ were taken from the MSISE-90 model. The CO₂ VMR corresponds to the mean profile retrieved in the CRISTA experiments *Kaufmann et al. (2002)*. It deviates from well mixed values between 70 and 80 km, and is significantly smaller above these altitudes than the profile obtained from earlier rocket-borne mass spectrometer experiments, in which c_{ν,CO_2} is constant up to 90 km. For each temperature model $T(z)$, 1000 individual $T'(z)$ profiles were randomly generated as described in *Kutepov et al. (2007)*. The non-LTE problem was solved and radiative cooling/heating $h(z)$ computed for each profile $T(z) + T'(z)$ and corresponding profiles $c_{\nu,M} + c'_{\nu,M}$ for $M = O(^3P)$, CO₂, where $c'_{\nu,M}$ were calculated following (1.4). The mean cooling $\overline{h(z)}$ was then ob-

tained by averaging $h(z)$ at each altitude z . It was compared with the cooling $h_T(z)$ for the mean temperature and the $O(^3P)$ and CO_2 VMR profiles .

1.5 Results and Discussion

In the Fig. 1.1(a) we show the employed VMRs of $O(^3P)$ (for SAW and MLW) and CO_2 as well as the temperature variance profile $\sigma_T(z) = \{\overline{[T'(z)]^2}\}^{1/2}$ (for MLW) computed from 1000 distributions of $T'(z)$. Panels (b) and (c) of this figure show $\Delta h(z) = \overline{h(z)} - h_T(z)$ for SAW and MLW, obtained for Case 1, discussed in detail by Kutepov *et al.* (2007), with only T' disturbances (solid green lines), for Case 2 with both T' and $[O(^3P)]'$ disturbances (solid blue lines), and for Case 3 with T' , $[O(^3P)]'$ and $[CO_2]'$ (solid red lines) accounted for. Accounting for $[O(^3P)]'$ increases additional cooling for SAW at 85–100 km (to about 1 K day^{-1} at 90 km). This increase is obviously related to the large positive gradient of the $O(^3P)$ VMR at these altitudes (see Fig. 1.1(a). According to (1.4), it causes intensive variations of $[O(^3P)]'$. On the other hand, additional taking into account $[CO_2]'$ for this model (Case 3) leads to an opposite effect: the cooling decreases between 88 and 110 km compared to the Case 2 to $\sim 1.7 \text{ K day}^{-1}$ at 95 km. The latter is related to the rapid fall of the CO_2 VMR at these heights (Fig. 1.1(a)) that causes significant negative gradient. Similar effects are seen for MLS (panel c): accounting for $[O(^3P)]'$ increases the cooling effect to about 1 K day^{-1} at 100 km, whereas the additional accounting for $[CO_2]'$ causes the warming up to about 2 K day^{-1} in the layer between 100 and 105 km. In the Case 3, the total effect changes its sign at about 100 km: the cooling reaching about 1 K day^{-1} at 89 km is accompanied by the warming of up to 1 K/day at 105 km.

In Fig. 1.1(d), additional cooling/heating is shown for the Cases 1 and 3 for all the 5 temperature models. One can see that compared to Case 1, accounting for $[O(^3P)]'$ and $[CO_2]'$ simultaneously with T' makes the total effect significantly more variable depending on peculiarities of temperature and VMR profiles. For instance, for MLW, SAW, TROP and SAS models the cooling is stronger (up to 0.7 K day^{-1} for SAW), however, the corresponding cooling maxima are now located at the altitudes which are few km lower than those when only variations of T' were taken into account. Additionally, a weak warming appeared for all considered models at 100–108 km reaching 0.8 K day^{-1} for MLS.

1.6 Parametrization

Eq. (6) in Kutepov *et al.* (2007) defines the radiative flux divergence for the fundamental transition of main CO_2 isotope 626, main contributor for the effect discussed above, as

$$h_{T,626FB}(z) = \chi \frac{C}{A+C} (J - B), \quad (1.6)$$

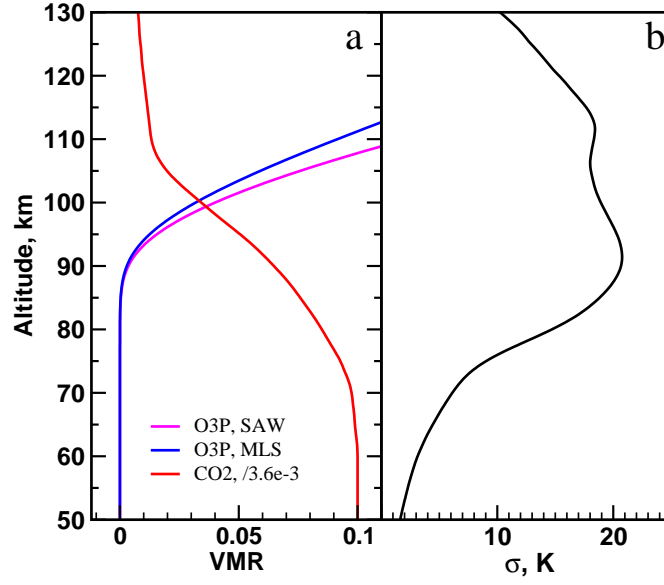


Fig. 1.1 a: VMRs of O(³P) and CO₂ used in this study (see text), and the temperature variance σ_T ; b: Δh for SAW model; c: Δh for MLS model; d: Δh for 5 atmospheric models: thick solid lines - this study; thin solid lines with diamonds - results of *Kutepov et al.* (2007).

where A and C are the Einstein coefficient for the spontaneous emission in the band and the total collisional quenching rate of the upper vibrational level, respectively; J is the mean radiative intensity in the band, B is the Planck function for the band center frequency ν_0 , and

$$\chi = \int \chi(\nu) d\nu = \frac{h\nu_0}{4\pi} B_{01} n_0 \sim B_{01} n_a c_{\nu, \text{CO}_2} \quad (1.7)$$

is the mean atmospheric opacity in the spectral band of fundamental transition (with neglect of the stimulated emission). In the latter equation, B_{01} is the Einstein absorption coefficient for the band, and n_0 is the population of the CO₂ vibrational ground level. With taking into account the low degree of the CO₂ vibrational excitation in the atmosphere, it is usually assumed that n_0 is approximately equal to the total CO₂ density $n_{\text{CO}_2} = n_a c_{\nu, \text{CO}_2}$, where n_a is the total atmospheric density, and c_{ν, CO_2} is the CO₂ VMR. In (1.6) the collisional quenching rate $C = kn_a$, where k is the total quenching rate coefficient, see (1.10) below.

Following the approach of *Kutepov et al.* (2007) we concentrate here on the analysis of the second term in (1.6) that describes the non-LTE emission of the volume unit. According to the analysis above, this term is proportional to $E = c_{\nu, \text{CO}_2} CB(T)$. Variations T' induce fluctuations c'_{ν, CO_2} and $c'_{\nu, \text{O}(\text{3P})}$, which are estimated according to (1.4). Averaging E over GW-induced fluctuations, one may obtain that

$$\overline{E} \approx [c_{v,\text{CO}_2} + \Delta c_{v,\text{CO}_2}][C + \Delta C]B(T + \Delta T), \quad (1.8)$$

where $\Delta c_{v,\text{CO}_2}$, ΔC , and ΔT depend on the temperature variance and gradients of c_{v,CO_2} and $c_{v,\text{O}(\text{}^3\text{P})}$

$$\begin{aligned} \Delta c_{v,\text{CO}_2} &= \frac{1.3e3 \varepsilon_{\text{CO}_2} \sigma_T^2}{T^2}, \quad \Delta c_{v,\text{O}(\text{}^3\text{P})} = \frac{8.9e2 \varepsilon_{\text{O}(\text{}^3\text{P})} \sigma_T^2}{T^2}, \\ \Delta T &= [4.8e2 \frac{1-2.1e-3T}{T^2} + 7e-2 \varepsilon_{\text{O}(\text{}^3\text{P})} \frac{k_{\text{O}(\text{}^3\text{P})}}{k}] \sigma_T^2, \end{aligned} \quad (1.9)$$

where

$$\begin{aligned} \sigma_T^2 &= \overline{(T')^2}, \\ k &= c_{v,\text{O}(\text{}^3\text{P})} k_{\text{O}(\text{}^3\text{P})} + c_{v,\text{N}_2} k_{\text{N}_2} + c_{v,\text{O}_2} k_{\text{O}_2}, \\ k_{\text{O}(\text{}^3\text{P})} &= 6e-12 \sqrt{\left(\frac{T}{300}\right)}, \\ k_{\text{N}_2} &= 5.5e-17 \sqrt{T} + 6.7e-10 \exp(-83.8 T^{-1/3}), \\ k_{\text{O}_2} &= 1e-15 \exp(23.37 - 230.9 T^{-1/3} + 564.0 T^{-2/3}). \end{aligned} \quad (1.10)$$

In (1.10), $k_{\text{O}(\text{}^3\text{P})}$ corresponds to that of *Sharma and Wintersteiner* (1990), whereas k_{N_2} and k_{O_2} are taken from *Shved et al.* (1998). Detailed derivation of $\Delta \dots$ is given in *Kutepov et al.* (2011). Note that with $\varepsilon_{\text{CO}_2}, \varepsilon_{\text{O}(\text{}^3\text{P})}=0$ (1.9) reduces to

$$\Delta T(z) = \frac{1.44 v_0}{2T^2(z)} \left[1 - \frac{2T(z)}{1.44 v_0} \right] \overline{[T'(z)]^2} \quad (1.11)$$

for $\Delta T(z)$ of *Kutepov et al.* (2007) with $v_0=667.4 \text{ cm}^{-1}$ for fundamental band of the CO_2 isotope 626.

In Fig. 1.1(c) and (d) we compare the rigorously computed Δh (solid blue and red curves) for SAW and MLS models with those obtained with T , c_{v,CO_2} and $c_{v,\text{O}(\text{}^3\text{P})}$ replaced with $T + \Delta T$, $c_{v,\text{CO}_2} + \Delta c_{v,\text{CO}_2}$ and $c_{v,\text{O}(\text{}^3\text{P})} + \Delta c_{v,\text{O}(\text{}^3\text{P})}$, respectively. Here $\Delta \dots$ corresponds to the parametrization (1.9). One can see in this figure that the expressions for $\Delta \dots$ allow for very accurate accounting of extra cooling/heating associated with the additional influence of $[\text{O}(\text{}^3\text{P})]'$ (blue dashed curves) as well with both $[\text{O}(\text{}^3\text{P})]'$ and $[\text{CO}_2]'$ variations included (red dashed curves). We tested (1.9) for the 5 temperature models, and found that the absolute error of applying these expressions does not exceed 0.4 K day^{-1} . The parametrization (1.9) demonstrates a high flexibility and allows accounting for a variety of atmospheric conditions. As in the case of pure temperature fluctuations studied in *Kutepov et al.* (2007), the effect is related to the strong temperature dependence of the Planck function B . In *Kutepov et al.* (2007), the linear with respect to T' term in the power expansion of B canceled out with averaging. However, in this study, it correlates with $[\text{O}(\text{}^3\text{P})]'$ and $[\text{CO}_2]'$, which both are $\sim T'$. As a result, the effect of subgrid variations turn out to be stronger and significantly more variable depending on the gradients of T , $\text{O}(\text{}^3\text{P})$ and CO_2 .

Above $\approx 85 \text{ km}$, the $\text{O}(\text{}^3\text{P})$ atoms begin to dominate the quenching of the CO_2 v_2 vibrations *Kutepov et al.* (2006). As the result, the CO_2 radiative cooling in this

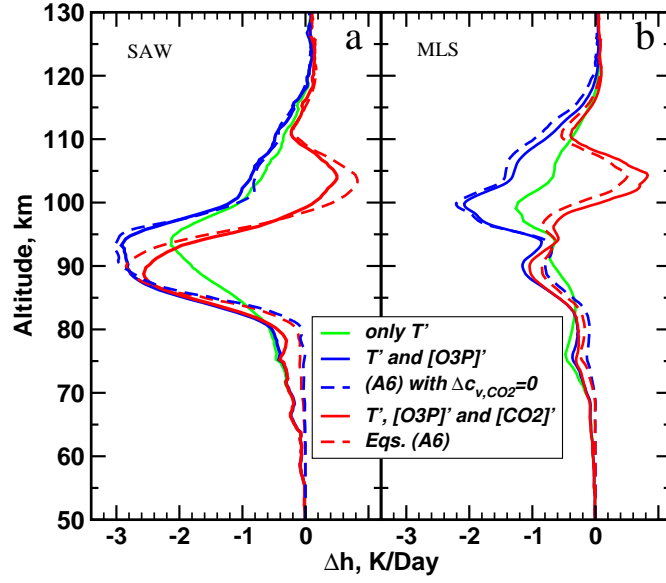


Fig. 1.2 a: VMRs of $O(^3P)$ and CO_2 used in this study (see text), and the temperature variance σ_T ; b: Δh for SAW model; c: Δh for MLS model; d: Δh for 5 atmospheric models: thick solid lines - this study; thin solid lines with diamonds - results of *Kutepov et al.* (2007).

region strongly depends on the product $[O(^3P)] \times k_{O(^3P)}$, which provides the atomic oxygen contribution to the total quenching rate C . Δh discussed above were obtained for the high value of quenching rate coefficient $k_{O(^3P)} = 6 \times 10^{-12} \text{ cm}^3 \text{ s}^{-1}$ (for $T=300^\circ \text{ K}$), retrieved from space observations of $15 \mu\text{m}$ emissions *Sharma and Wintersteiner* (1990). Application of the lower $k_{O(^3P)} = 1.5 \times 10^{-12} \text{ cm}^3 \text{ s}^{-1}$, which is more consistent with recent laboratory measurements *Castle et al.* (2006), reduces the maximum values of the additional cooling shown in Fig. 1.1(d) by a factor of about 2 following the drop of the ratio $C/(C+A)$ in (1.6) for these altitudes when $k_{O(^3P)}$ is replaced with $k_{O(^3P)}/4$.

1.7 Effects of ITFs on the O_3 and H_2O Cooling

Following the calculation procedure described in Sec. 1.4 we also applied the ALI-ARMS code for 5 selected atmospheric models to estimate the effect subgrid T' on the cooling of the MLT in the O_3 $9.6 \mu\text{m}$ and the H_2O rotational bands. $[O_3]$ for these calculations were taken from the SABER V1.07 data product. $[H_2O]$ were those from the HALOE V19 data product. The H_2O rotational band is in LTE throughout the MLT, whereas the O_3 $9.6 \mu\text{m}$ band departs from LTE above the altitude of 65–70 km. We utilized the model of non-LTE in O_3 developed by *Manuilova*

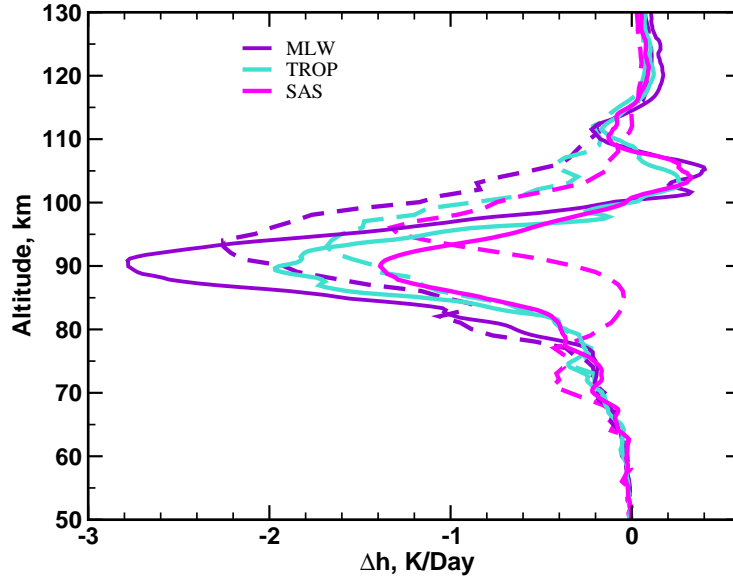


Fig. 1.3 a: VMRs of $O(^3P)$ and CO_2 used in this study (see text), and the temperature variance σ_T ; b: Δh for SAW model; c: Δh for MLS model; d: Δh for 5 atmospheric models: thick solid lines - this study; thin solid lines with diamonds - results of Kutepov *et al.* (2007).

et al. (1998). It was found that the O_3 9.6 μm additional cooling caused by subgrid T' reached between 90 and 100 km 0.3, 0.24, 0.15, 0.1 and 0.05 $K day^{-1}$ for the SAW, MLW, TROP, MLS, and SAS models, respectively. The same effect for the H_2O rotational band did not exceed 0.05 K/day for all the models considered. We also found that the additional cooling can be well accounted for by correcting the input temperature by means (1.11) with $\nu_0=1043$ and $500 cm^{-1}$ for O_3 and H_2O , respectively.

1.8 Application in the LIMA Model

To estimate the effects of the GW-induced CO_2 cooling, we implemented the parametric expressions (??) into the Leibniz Institute Middle Atmosphere (LIMA) GCM, which was described in detail in [Berger, 2008]. The peculiarity of the model is that its dynamical core employs a triangle grid with more than 42000 edge points over the globe with a distance between grids of about 110 km. Together with a relatively small vertical grid step of about 1.1 km this allows to resolve a significant portion of GWs and avoid using GW parametrization. Radiative calculations are performed on a much coarser grid (16×36 in the longitude and latitude directions respectively) with vertical grid step of about 1.8 km. Typically, about 20 or more triangles are located inside such a latitude-longitude segment. The background

fields required for the radiative CO₂ scheme are the averaged over each bin with 20 and more points. We attribute the deviations from the mean fields within a bin to GWs, and, therefore, were able to calculate the temperature variance $\sigma_T = (\overline{T'^2})^{1/2}$ corresponding to the bin. This variance, however, corresponds to GWs resolved by LIMA, $\sigma_{T,res}$ whereas our aim is to estimate the variance of subgrid-scale harmonics unresolved by the model, $\sigma_{T,unres}$. To relate $\sigma_{T,unres}$ to $\sigma_{T,res}$, we performed calculations with our stochastic model of GW-like disturbances [Kutepov *et al.*, 2007], and estimated for 5 atmospheric models variances produced by 1000 harmonics with vertical wavelengths between 2 and 11 km, and those with wavelengths between 6 and 11 km. The former set is referred to as “all GW spectrum”, whereas the second set as the “resolved GW spectrum”. This implies that waves shorter than 6 km are considered as unresolved by LIMA due to the reasons discussed in the Introduction. Since the temperature variance is the sum of variances of the resolved and unresolved parts of GW spectra, we thus were able to calculate $\sigma_{T,unres}$ from these two variances. The mean for 5 atmospheric models ratio of the “unresolved” and “resolved” rms temperature fluctuations is given in Figure 1.4. It is seen that between 80 and 100 km, the height interval where the effect of additional CO₂ cooling is most considerable, this ratio varies between 5 and slightly less than 2.

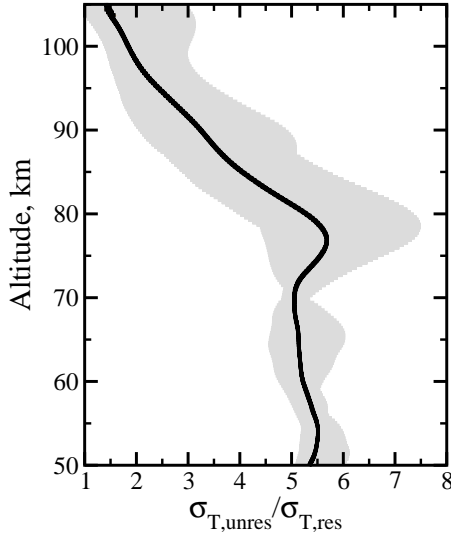


Fig. 1.4 The ratios of the “unresolved” and “resolved” rms temperature fluctuations. Gray patten: corridor of ratio values for 5 atmospheric models used in this study (see text for details). Black solid line: mean ratio for 5 atmospheric models.

In our LIMA simulations we used in parametric expressions (??) $\sigma_T = \sigma_{T,unres} = 2 \times \sigma_{T,res}$ as a modest estimate of the subgrid GW-induced rms temperature fluctuations, where $\sigma_{T,res}$ is the variance of resolved GWs calculated as described above.

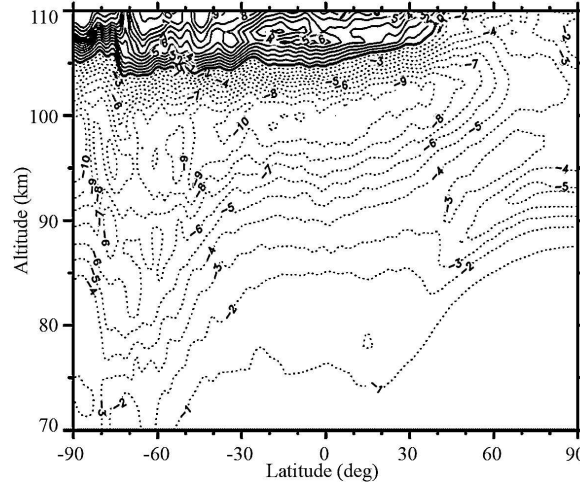


Fig. 1.5 Differences of simulated monthly and zonal mean temperatures for July 2005 obtained with and without accounting for the additional IR CO₂.

The calculations were performed with $k_{\text{O}(^3\text{P})} = 6 \times 10^{-12} \text{ cm}^3 \text{ s}^{-1}$ (for $T=300^\circ \text{ K}$) of [Sharma and Wintersteiner, 1990].

The effects of the additional cooling on temperature are presented in Figure ?? for the monthly and zonal mean temperatures for July 2005. It is seen in that sub-grid ITFs cause warming above about 105 km and cooling below at latitudes between 90°S and 40°N . In the winter hemisphere, the effects are larger due to the larger GW activity. The simulated polar summer mesopause region turns out to be broader and colder when the additional cooling is accounted for. The difference reaches appreciable values of about of 5–6 K. Thus simulated temperature in the region as well as in the transition to the lower thermosphere layer is more consistent with the recent lidar

We implemented the parametric expressions (1.9) into the Leibniz Institute Middle Atmosphere (LIMA) GCM Berger (2008) to estimate the effects of the subgrid (for waves shorter than 6 km) GW-induced CO₂ cooling. Details of this implementation are described by Kutepov et al. (2011). The effects of additional cooling/heating on temperature are presented in Fig. 1.5 for the monthly and zonal mean temperatures for July 2005. It is seen in that sub-grid ITFs cause warming above about 105 km and cooling below at latitudes between 90°S and 40°N . In the winter hemisphere, the effects are larger due to the larger GW activity. The simulated polar summer mesopause region turns out to be broader and colder when the additional cooling is accounted for. The difference reaches appreciable values of about of 5–

6 K. Thus simulated temperature in the region as well as in the transition to the lower thermosphere layer is more consistent with the recent lidar measurements at Spitsbergen Höffner and Lübken (2007).

1.9 Conclusion

In this study we analyzed additional cooling/heating of MLT in the infra-red bands of CO₂ O₃ and H₂O caused the subgrid GWs. We applied a statistical model of GWs to perform direct calculations of the infra-red cooling/heating taking into account the non-LTE. The results show that additional cooling/heating is very variable depending on peculiarities of temperature and VMR profiles. In the periods of strong GW activity it can produce an additional cooling up to 4 K day⁻¹ near the mesopause. A simple parametrization has been derived that computes corrections depending on the temperature fluctuations variance of subgrid GWs, which should be added in radiative calculations to the mean temperature, CO₂ and O(³P) VMR profiles to account for the additional cooling associated with the unresolved disturbances. Implementation of this scheme into the LIMA model resulted in a colder and broader simulated summer mesopause in agreement with recent lidar measurements at Spitsbergen.

Finally we note, that corrections (1.9) depend on the mean variance of temperature perturbations, $\overline{[T'(z)]^2}$. For applications in GCM, this quantity can be obtained from GW parameterizations which normally calculate the wind variance for GW fluctuations, $\overline{[u(z)]^2}$. The variance $\overline{[T'(z)]^2}$ can readily be computed from the variance $\overline{[u'(z)]^2}$ with the help of the polarization relations for GW.

References

- Berger, U. (2008), Modeling of middle atmosphere dynamics with LIMA, *J. Atmos. Solar-Terr. Phys.*, *70*, 1170–1200, doi:10.1016/j.jastp.2008.02.004.
- Brasseur, G. P., and S. Solomon (2005), *Aeronomy of the Middle Atmosphere: Chemistry and Physics of the Stratosphere and Mesosphere*, Springer.
- Castle, K. J., K. M. Kleissas, J. M. Rhinehart, E. S. Hwang, and J. A. Dodd (2006), Vibrational relaxation of CO₂(v₂) by atomic oxygen, *J. Geophys. Res.*, *111*, A09,303, doi:10.1029/2006JA011736.
- Fritts, D. C., and M. J. Alexander (2003), Gravity wave dynamics and effects in the middle atmosphere, *Annals of Geophysics*, *41*(1), 1003–1066, doi: 10.1029/2001RG000106.
- Gusev, O. A., and A. A. Kutepov (2003), Non-LTE gas in planetary atmospheres, in *Stellar Atmosphere Modeling, Astronomical Society of the Pacific Conference Series*, vol. 288, edited by . K. W. I. Hubeny, D. Mihalas, pp. 318–330.

- Höffner, J., and F.-J. Lübken (2007), Potassium lidar temperatures and densities in the mesopause region at spitsbergen (78_{degN}), *J. Geophys. Res.*, *112*, D20,114, doi:10.1029/2007JD008612.
- Kaufmann, M., O. A. Gusev, K. U. Grossmann, R. G. Roble, M. E. Hagan, C. Hart-sough, and A. A. Kutepov (2002), The vertical and horizontal distribution of CO_2 densities in the upper mesosphere and lower thermosphere as measured by crista, *J. Geophys. Res.*, *107*, 8182, doi:10.1029/2001JD000704.
- Kutepov, A. A., O. A. Gusev, and V. P. Ogibalov (1998), Solution of the non-lte problem for molecular gas in planetary atmospheres: superiority of accelerated lambda iteration., *J. Quant. Spectrosc. Radiat. Transfer*, *60*, doi:10.1016/S0022-4073(97)00167-2.
- Kutepov, A. A., A. G. Feofilov, B. T. Marshall, L. L. Gordley, W. D. Pesnell, R. A. Goldberg, and J. M. Russell (2006), Saber temperature observations in the summer polar mesosphere and lower thermosphere: Importance of accounting for the CO_2 v_2 quanta v-v exchange, *Geophys. Res. Lett.*, *33*, L21,809, doi: 10.1029/2006GL026591.
- Kutepov, A. A., A. G. Feofilov, A. S. Medvedev, A. W. A. Pauldrach, and P. Hartogh (2007), Small-scale temperature fluctuations associated with gravity waves cause additional radiative cooling of the mesopause region, *Geophys. Res. Lett.*, *34*, L24,807, doi:10.1029/2007GL032392.
- Kutepov, A. A., A. G. Feofilov, A. S. Medvedev, U. Berger, and M. Kaufmann (2011), Radiative cooling of the mesopause region due to small-scale fluctuations of temperature, $[\text{O}(^3\text{P})]$ and $[\text{CO}_2]$ associated with gravity waves, , *submitted to Geophys. Res. Lett.*
- Manuilova, R. O., O. A. Gusev, A. A. Kutepov, T. von Clarmann, H. Oelhaf, G. P. Stiller, A. Wegner, M. López Puertas, F. J. Martín-Torres, G. Zaragoza, and J. M. Flaud (1998), Modelling of non-LTE limb radiance spectra of IR ozone bands for the MIPAS space experiment, *J. Quant. Spectrosc. Radiat. Transfer*, *59*, 405–422, doi:10.1016/S0022-4073(97)00120-9.
- Sharma, R. D., and P. P. Wintersteiner (1990), Role of carbon dioxide in cooling planetary thermospheres, *Geophys. Res. Lett.*, *17*, 2201–2204, doi: 10.1029/GL017i012p02201.
- Shved, G. M., A. A. Kutepov, and V. P. Ogibalov (1998), Non-local thermodynamic equilibrium in CO_2 in the middle atmosphere. I. Input data and populations of the v_3 mode manifold states, *JASTP*, *60*, 289–314, doi:10.1016/S1364-6826(97)00076-X.
- Ward, W. E. (1999), A simple model of diurnal variations in the mesospheric oxygen nightglow, *Geophys. Res. Lett.*, *26*(23), 3565–3568, doi:10.1029/1999GL003661.